Journal of
Applied Physics

Control of interlayer physics in 2H transition metal dichalcogenides EP

Cite as: J. Appl. Phys. **122**, 224302 (2017); https://doi.org/10.1063/1.5005958
Submitted: 20 September 2017 . Accepted: 03 November 2017 . Published Online: 11 December 2017

Kuang-Chung Wang, Teodor K. Stanev, Daniel Valencia, James Charles, Alex Henning, Vinod K. Sangwan, Aritra Lahiri, Daniel Mejia, Prasad Sarangapani, Michael Povolotskyi, Aryan Afzalian, Jesse Maassen, Gerhard Klimeck, Mark C. Hersam, Lincoln J. Lauhon, Nathaniel P. Stern, and Tillmann Kubis

COLLECTIONS

EP This paper was selected as an Editor's Pick

ARTICLES YOU MAY BE INTERESTED IN

Graphene and related two-dimensional materials: Structure-property relationships for electronics and optoelectronics
Applied Physics Reviews **4**, 021306 (2017); https://doi.org/10.1063/1.4983646

Tutorial: Novel properties of defects in semiconductors revealed by their vibrational spectra
Journal of Applied Physics **123**, 161561 (2018); https://doi.org/10.1063/1.5011036

2D-2D tunneling field-effect transistors using $WSe_2/SnSe_2$ heterostructures
Applied Physics Letters **108**, 083111 (2016); https://doi.org/10.1063/1.4942647

J. Appl. Phys. **122**, 224302 (2017); https://doi.org/10.1063/1.5005958 **122**, 224302

AIP Publishing

JOURNAL OF APPLIED PHYSICS **122**, 224302 (2017)

Control of interlayer physics in 2H transition metal dichalcogenides

Kuang-Chung Wang,[1,a)] Teodor K. Stanev,[2] Daniel Valencia,[1] James Charles,[1]
Alex Henning,[3] Vinod K. Sangwan,[3] Aritra Lahiri,[1,4] Daniel Mejia,[1] Prasad Sarangapani,[1]
Michael Povolotskyi,[5] Aryan Afzalian,[6] Jesse Maassen,[7] Gerhard Klimeck,[1,5,8]
Mark C. Hersam,[3,9] Lincoln J. Lauhon,[3] Nathaniel P. Stern,[2] and Tillmann Kubis[1,5,8]
[1]*School of Electrical and Computer Engineering, Purdue University, West Lafayette, Indiana 47906, USA*
[2]*Department of Physics and Astronomy, Northwestern University, Evanston, Illinois 60208, USA*
[3]*Department of Materials Science and Engineering, Northwestern University, Evanston, Illinois 60208, USA*
[4]*Department of Electrical Engineering, IIT Bombay, Mumbai, India*
[5]*Network for Computational Nanotechnology, Purdue University, West Lafayette, Indiana 47906, USA*
[6]*TSMC, Kapeldreef 75, 3001 Leuven, Belgium*
[7]*Department of Physics and Atmospheric Science, Dalhousie University, Halifax, Nova Scotia B3H 4R2, Canada*
[8]*Purdue Center for Predictive Materials and Devices, Purdue University, West Lafayette, Indiana 47906, USA*
[9]*Department of Chemistry, Northwestern University, Evanston, Illinois 60208, USA*

(Received 20 September 2017; accepted 3 November 2017; published online 11 December 2017)

It is assessed in detail both experimentally and theoretically how the interlayer coupling of transition metal dichalcogenides controls the electronic properties of the respective devices. Gated transition metal dichalcogenide structures show electrons and holes to either localize in individual monolayers, or delocalize beyond multiple layers—depending on the balance between spin-orbit interaction and interlayer hopping. This balance depends on the layer thickness, momentum space symmetry points, and applied gate fields. The design range of this balance, the effective Fermi levels, and all relevant effective masses is analyzed in great detail. A good quantitative agreement of predictions and measurements of the quantum confined Stark effect in gated MoS_2 systems unveils intralayer excitons as the major source for the observed photoluminescence. *Published by AIP Publishing.* https://doi.org/10.1063/1.5005958

I. INTRODUCTION

Transition metal dichalcogenides (TMDs) are expected to push nanotechnology to the ultimate scaling limit of one or a few atoms only. In contrast to graphene, these 2D materials maintain a native bandgap that is essential for most electronic device applications. TMD based devices have excellent sensitivity to external fields.[1–3] Obvious ultrascaled applications range from sensing (e.g., Refs. 4–7), lighting (e.g., Refs. 8–10), logic devices (e.g., Refs. 11 and 12), and wearable electronics (e.g., Refs. 13 and 14).

The weak van der Waals coupling between TMD layers allows for low cost fabrication (with micro-mechanical cleavage[15]) and stacking of different TMD materials on top of each other which significantly widens the material design space.[16,17] A critical question for most TMD systems is the nature of the coupling between TMD layers. The properties of TMD materials can be tuned via the number of coupled layers. For instance, the band-gap of MoS_2 varies by about 1 eV and switches between direct and indirect when the thickness changes.[3] These features suggested to combine TMD layers of different thicknesses and materials to improve, e.g., tunneling field effect transistors.[18,19]

In spite of the importance of the interlayer coupling, its detailed properties and dependencies are not fully assessed, yet. For instance, recent experiments on excitons in TMD materials raised the question whether electron hole recombinations are predominantly within the same or between different TMD layers.[20,21] Depending on the experimental setup, interlayer excitons appear in photoluminescence measurements, while intralayer transitions yield either a finite or a vanishing Stark effect.[22,23] Given the varying findings in the literature, a comparative study of experiments and realistic theoretical models is needed to conclusively assess the interlayer coupling. This is the core purpose of this work.

Although the main focus of this work is the theoretical assessment of the interlayer physics, the reliability of the theoretical answers is assessed with quantitative comparisons of predicted quantum confined Stark effects with experimental observations in various gated MoS_2 structures.

All TMD devices in this work are subatomically resolved. *Ab-initio* electronic Hamiltonian operators are discretized with maximally localized Wannier functions (MLWFs).[24] This treatment combines numerical efficiency with the best known physical accuracy.[25] In contrast to pure *ab-initio* models,[22] this approach allows to realistically include the presence of electric gates, thickness dependent doping, and dielectric constants. Charge effects turn out to significantly influence the interlayer coupling. Commonly, electronic charge distributions are interpreted point-like within the discretization of the Poisson equation.[26] It is an important aspect of this work that these charges are resolved in the subatomic resolution as well. These features guarantee full transferability of the electronic model[25,27] to device dimensions that are computationally inaccessible to the pure

---

[a)]Electronic mail: wang2366@purdue.edu

density functional theory (DFT) applications.[28] Note that important device aspects such as doping densities and spatially varying gate control are beyond the scope of pure DFT applications otherwise.[29]

All fabricated devices of this work consist of varying numbers of TMD layers placed on SiO_2 and highly p-doped Si that serves as the gate electrode. Our calculations show that both interlayer and intralayer excitons yield Stark effects. However, intralayer transitions are about 2 orders of magnitude less likely. Our experimental data and theoretical predictions for the Stark effect of intralayer transitions agree well. Both theory and experiments do not show significant interlayer transitions.

The paper is organized as follows: in Section II, the details of the theoretical model and experimental setup are given. Section III first confirms the transferability of the electronic band structure model to the considered devices. It then illustrates and discusses wave function and band structure properties and their dependence on the balance of spin-orbit interaction and interlayer coupling strength. This balance depends on the layer thickness, electronic momentum, and applied gate fields. The comparison of calculated band gap changes with experimentally observed photoluminescence data confirms Stark effects for both inter and intra layer direct band gap excitons. In agreement with the literature, intralayer excitons are found to be significantly more visible.

II. METHOD

A. Experiment

The device fabrication followed the procedure of Ref. 15. MoS_2 samples were mechanically exfoliated from bulk MoS_2 crystals and put on 285 nm thick SiO_2 layers that were grown on p-doped silicon substrates (see the schematic in Fig. 1). Suitable multilayer samples were identified by optical microscopy and their thickness was confirmed independently through atomic-force microscopy. All fabricated samples were first annealed at 300 °C to remove the residue from the exfoliation process in an Ar/H2 environment (800/200 sccm). The electrostatic gates were defined through e-beam lithography on a MMA/PMMA mask, followed by 100 nm deposition of Au via thermal evaporation. Next, the devices were annealed at 200 °C (800/200 sccm, Ar/H2) to clean the substrate of the polymer residue from fabrication and improve the contact between metals and semiconductor layers before being loaded into a closed-cycle optical cryostat (Advanced Research Systems DMX-20-OM)[30] and pumped down to high vacuum at 10^{-7} mbar. The devices were kept at 350 K for about 6 h in high vacuum while laser annealing was applied with a 5 mW beam of a 100 μm spot size. This was meant to help remove atmospheric contaminants, before the samples were cooled down to 10 K, i.e., the temperature at which all measurements were conducted. Photoluminescence measurements were performed using a continuous pump laser beam of 532 nm wavelength with a laser power of 40 μW and a spot size of 2 μm. The emitted light was analyzed with an Andor Shamrock Spectrograph[31] using a 150 lines/mm grating.

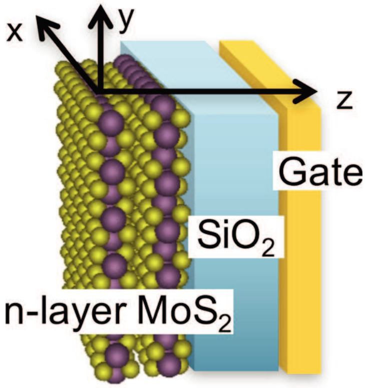

FIG. 1. Schematics of the metal-oxide semiconductor structure considered in this paper. The MoS_2 structure varies in thickness and is limited to the right by the gate and to the left by vacuum.

B. Model

The atomic structures of all TMD layers modelled in NEMO5[32] (i.e., MoS_2, WTe_2, WS_2, WSe_2, and $MoSe_2$) are based on the relaxation calculations of the respective infinite number of layer systems in the trigonal prismatic polytype (i.e., in the 2H symmetry)[3] performed in the DFT tool VASP[33] with the self-consistent electronic model and the convergence criterion of 1×10^{-8} eV. A momentum mesh of $5 \times 5 \times 5$ Monkhorst-Pack grids and an energy cutoff of 520 eV are used along with van der Waals force included according to Ref. 34. The lattice constants deduced from these DFT based relaxation calculations are given in Table I and agree well with the findings in Refs. 35 and 36. The applied DFT model is based on the generalized gradient approximation utilizing the Perdew-Burke-Ernzerhof functionals.[37] The electronic DFT Hamiltonian is transformed into an MLWF representation using the Wannier90 software[38–40] with *d* orbitals for the metal electrons and sp^3 orbitals for the chalcogenide electrons as the initial projection. The spreading of the Wannier functions[24] is reduced iteratively until it converges to around 2 Å^2. The atom positions and their corresponding electronic Hamiltonian of finite TMD structures are then created in NEMO5 (Ref. 32) as portions of the respective infinite system. As a consequence, all TMD systems in this work are intralayer periodic (in the x- and y-direction of the schematic in Fig. 1) with the Bloch boundary conditions applied. Nonlocal Hamiltonian elements are considered up to the material specific range listed in Table I. All calculations of gated MoS_2 structures

TABLE I. Structure parameters of all TMD materials resulting from the relaxation and parameterization algorithm described in the main text.

	u (Å)	a (Å)	c (Å)	Range (Å)
MoS_2	3.12	3.18	12.48	20
$MoSe_2$	3.34	3.32	13.14	25
WS_2	3.15	3.19	12.49	23
$MoTe_2$	3.62	3.56	14.22	26
WSe_2	3.36	3.33	13.24	26

sketched in Fig. 1 are performed with self-consistent solutions of the Schrödinger and Poisson equations. The Poisson equation is discretized on a finite element mesh (FEM). The resulting electrostatic potentials converged for FEM resolutions of 0.6 Å or better. The electronic density resulting from the solution of the Schrödinger equation is transformed into real space simplifying the MLWF basis with Gaussian functions with $\sigma = 0.68$ Å [in Eq. (1)]. This simplification eases the numerical burden during the iterative solution of the Poisson and the Schrödinger equation significantly and does not noticeably alter the actual spatial charge distribution as illustrated in Fig. 2. Figure 2 shows the integrated charge contribution function $P(r_0)$ in Eq. (2) solved with the charge distribution function $\rho(r,\theta,\phi)$ of the MLWF and the fitted Gaussian function $\rho_G(r,\theta,\phi)$ of Eq. (1), respectively,

$$\rho_G(r,\theta,\phi) = \frac{1}{\sqrt{8\sigma^6\pi^3}}\exp\left(-\frac{r^2}{\sigma^2}\right), \tag{1}$$

$$P(r_0) = \frac{\int_0^{\pi}\int_0^{2\pi}\int_0^{r_0}\rho(r,\theta,\phi)r^2\sin\phi\, dr d\theta d\phi}{\int_0^{\pi}\int_0^{2\pi}\int_0^{\infty}\rho(r,\theta,\phi)r^2\sin\phi\, dr d\theta d\phi}. \tag{2}$$

The MoS_2 thickness of the gated structure in Fig. 1 is varied between one and ten layers. In these cases, the donor doping is set to $1.5\times10^{18}\,\mathrm{cm}^{-3}$ for MoS_2 monolayers and $2\times10^{19}\,\mathrm{cm}^{-3}$ for 6 MoS_2 layers. The effective doping is induced from the atmospheric adsorbates. Their values are deduced from the experimental threshold voltages and gate oxide capacitances.[41] The doping density is linearly interpolated for MoS_2 layer systems in between 1 and 6 layers, and it is assumed to be saturated for MoS_2 layers thicker or equal to 6-layers.[41] As commonly done in device calculations,[42] the computational burden of 285 nm thick SiO_2 as the gate dielectric is avoided with a 12 nm dielectric slab of the same equivalent capacitance in the Poisson equation. SiO_2 did not enter the electron density calculations. The gate is considered as a Schottky contact with a metal work function of 5.15 eV (Ref. 43) for the highly p-doped Si. The energy offset is set to the Fermi level of the device electrons. The uncapped TMD side is considered to be exposed to the vacuum, modeled with the vanishing field boundary conditions for the Poisson equation. The MoS_2 dielectric constant is assumed to be homogeneous but linearly varying with the layer thickness following Ref. 44. The electronic wave functions of the conduction and the valence band states are used to solve the optical transition matrix elements. The peaks in these optical elements are considered as optical transition energies.[45] For all gate-independent band structures and wave function assessments in this work, a constant doping of $1.5\times10^{18}\,\mathrm{cm}^{-3}$ is assumed and the Fermi level is chosen to achieve local charge neutrality for the respective systems. The electron hole recombination energies are extracted from single particle band structures. As discussed in Ref. 46, many particle effects are expected to have in low order no net impact on the transition energies.

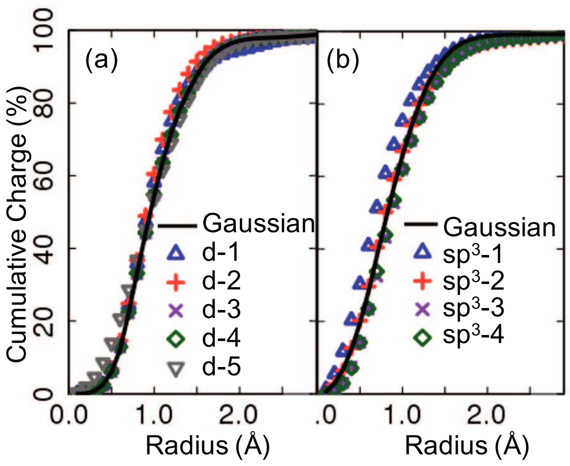

FIG. 2. Integrated charge contribution function $P(r_0)$ as defined in Eq. (2) as a function of the integration radius for orbitals of molybdenum (a) and sulfur (b) atoms in infinitely thick MoS_2. The black lines show $P(r_0)$ when the orbital wave functions are approximated with Gaussian functions of $\sigma = 0.68$ Å (a) and $\sigma = 0.6$ Å (b), respectively.

III. RESULTS

A. Transferability of MLWF parameters

The NEMO5-calculated band structures in the MLWF representation agree well with the ab-initio results of the VASP software[3] for any MoS_2 layer thickness (see Fig. 3 for the monolayer and 5-layer cases). A very similar transferability of the MLWF representation and fitting procedure was found for all other TMD materials and layer thicknesses. This is remarkable, since MLWF parameterizations are sometimes created for each material thickness individually.[25]

B. Conduction and valence band energies and masses

The conduction band minimum in 2D momentum space for monolayer and 5-layer MoS_2 is shown in Fig. 4. For all TMDs considered in this work, the lowest conduction band hosts valleys at the K points and close to the Q points, respectively. Note that each K-point (Q-point) contributes to 3 (1) Brillouin zones and therefore its valley is twofold (sixfold) degenerate. Similarly, all considered TMDs show two valleys in the highest valence band at the Γ point and at the K-point.[3] The relative energies of all these valleys depend on the layer thicknesses, as illustrated in Figs. 5(a)

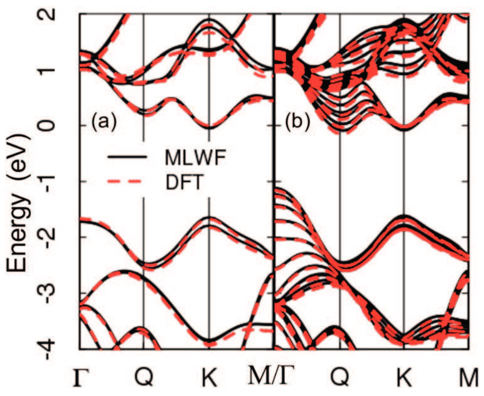

FIG. 3. Comparison of mono-layer (a) and quintuple layer (b) MoS_2 band diagrams solved with MLWF in NEMO5 and the DFT functionality of VASP. The agreement confirms the transferability of the MLWF parameters.

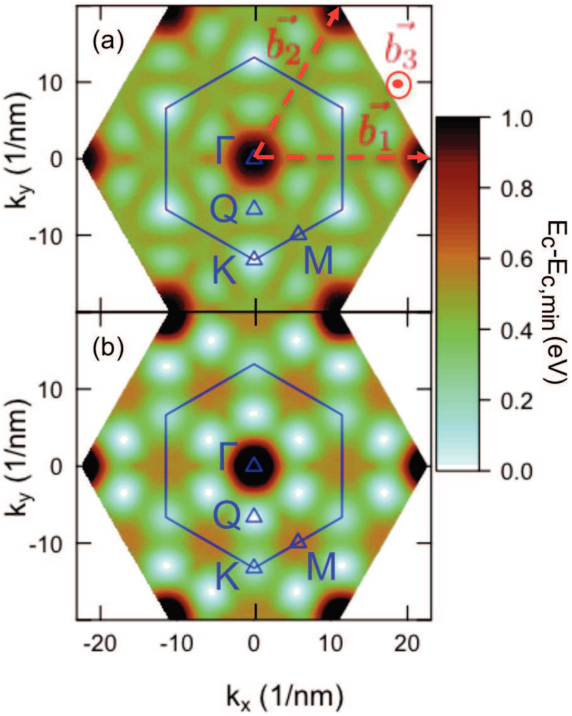

FIG. 4. Contour graph of the conduction band minimum of mono-layer (a) and 5-layer (b) MoS_2. The blue hexagon depicts the first Brillouin zone. The reciprocal lattice vectors are labeled with $\vec{b_1}$, $\vec{b_2}$, and $\vec{b_3}$. Note that the location of the Q valley is close to the middle between K and Γ.

and 5(b) for conduction and valence bands, respectively. Most of the TMDs show a transition of the conduction band minimum (valence band maximum) from the K to Q (K to Γ) valley at around 2 layer thickness.[47,48] The valley effective masses change with layer thickness as well (see Fig. 6)—very similar to findings of Ref. 3 for MoS_2.

C. Band edge density of states (DOS)

For a 2D system, the density of states (DOS) will be proportional to the effective mass. Note that the Q valley conduction band DOS decreases for all TMDs with increasing layer thickness as a direct consequence of the effective mass behavior. In the valence band, the Γ valley effective masses decay with the thickness, while the K valley masses stay fairly constant [see Figs. 6(c) and 6(d)]. The energies of K- and Q-valleys for two layer n-type TMDs are close enough so that both valleys contribute to the DOS at the band edge. Once the Q-valley of n-type TMDs [i.e., MoS_2,[49] $MoSe_2$,[50] and WS_2 (Ref. 51)] is significantly lower in energy than the K-valley (e.g., for more than 2 layers in the case of MoS_2), the DOS at the conduction band edge reduces with increasing layer thickness following the effective mass trend. This is exemplified in Fig. 7 which shows the DOS of MoS_2 with varying layer thickness.

To illustrate the DOS behavior for all considered n-type (p-type) TMDs and thicknesses, Fig. 8(a) [Fig. 8(b)] shows the effective Fermi level $E_f - E_c$ $(E_v - E_f)$ assuming a constant electron (hole) density of $1.5 \times 10^{18}\,\mathrm{cm}^{-3}$. Note that the larger the electron (hole) DOS is around the conduction band minimum (valence band maximum), the lower the effective Fermi level will be to maintain the assumed density. All n-type TMDs except WS_2 show a maximum DOS at 2 layers thickness when both K- and Q-valleys contribute. The p-type TMDs show a maximum DOS at 2 and 4 layers for $MoTe_2$ and WSe_2, respectively. This is the situation

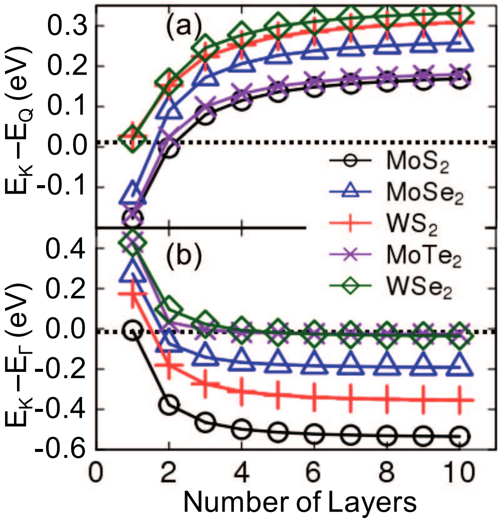

FIG. 5. Valley energy differences in the conduction band (K and Q valley) (a) and valence band (K and Γ valley) (b) as a function of the TMD layer thickness.

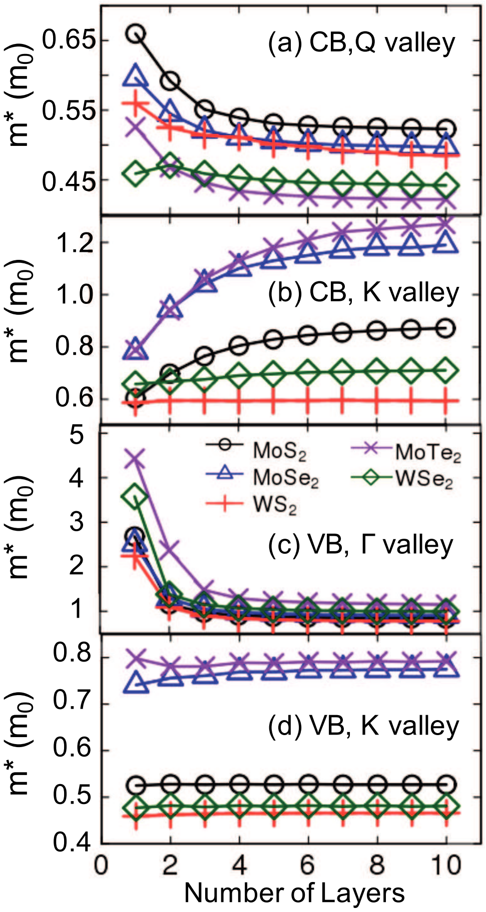

FIG. 6. Calculated effective masses along the $\vec{b_1} - 2\vec{b_2}$ direction for the conduction band Q (a) and K valley (b), as well as for the valence band Γ (c) and K valley (d).

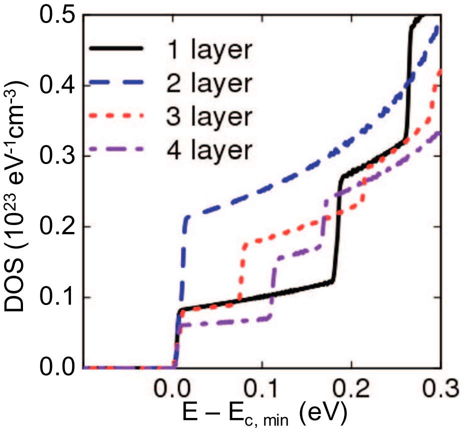

FIG. 7. Conduction band density of states in MoS_2 layers of various thicknesses. The 2 layer system has the largest DOS due to the alignment of K and Q conduction band valleys. Each step in the DOS marks an onset of a higher conduction band. The finite slope of the DOS between each step originates from a non-parabolic band dispersion.

when both the Γ and the *K* valleys similarly contribute to the DOS around the Fermi level.

D. Interlayer hybridization

2H-phase TMDs consist of alternating layers with 2 different orientations of metal-chalcogenide bonds (differing in a 60° rotation).[52,53] If the electrons are subjected to a pronounced spin-orbit interaction (e.g., in odd-layer 2H-TMD systems without an inversion symmetry[53–56]), the electronic states spreading across alternating layers are suppressed.[57,58] In contrast, the geometrical confinement favors the electronic states that are spread across the total device if the interlayer coupling is strong enough.[59] Figure 9 shows the band structure of an infinite layer $MoTe_2$ system at various symmetry points of the 2D momentum space along the $\vec{b_3}$ direction. The stronger the interlayer coupling, the strongly curved the respective bands in Fig. 9 are. In Fig. 9, several points in the band structure are labeled. They face different balances between the interlayer coupling strength and the spin-orbit interaction: At the valence band Γ point [labeled with (a)], the spin-orbit interaction vanishes and only the interlayer coupling determines the shape of the electronic wave functions. Here, this coupling is significant and gives an effective mass of $-2.31m_0$ for the top of the valence band. Consequently, the highest valence band states resemble typical infinite-barrier quantum well shapes [note they are spin degenerate, see Fig. 10(a)]. At the Q-point of the conduction band [labeled with (b) in Fig. 9], the spin-orbit interaction is finite but smaller than the strong interlayer coupling (effective mass $m^* = 0.53$ m_0 at Q along the $\vec{b_3}$ direction). Consequently, the shape of the electronic states shown in Fig. 10(b) is still comparable with those of Fig. 10(a), but the spin degeneracy is lifted. The top-valence band states at the K-point [labeled (c) in Fig. 9], face a similarly strong interlayer coupling (effective mass $m^* = -1.68m_0$ at K along the K-H direction) and spin-orbit interaction. Consequently, the respective wave functions avoid spreading in alternating layers. Instead, the states of equivalent layers (i.e., next-nearest neighbor layers) hybridize into bonding and anti-bonding states. In the case of a 3-layer system, the states of only two layers can follow that [depicted in Fig. 10(c) with circles for the bonding state and crosses for the antibonding state], while states of the center layer [symbol "+" in Fig. 10(c)] are effectively isolated. In agreement with Ref. 53, the lowest conduction band states at the K-point [labeled with (d) in Fig. 9] are found to have a very small interlayer coupling (effective mass $m^* = -699m_0$ at K along the $\vec{b_3}$ direction), i.e., a coupling smaller than the respective spin-orbit interaction. Therefore, the electronic states of individual layers barely interact and are effectively degenerate. Note that the spin-orbit interaction does not play a significant role in systems with an inversion symmetry (i.e., with an even number of layers). Very small spin-orbit coupling effects observed in these systems can be addressed to small p-orbital contributions of chalcogenide atoms to the conduction band.[55] Then, wave functions are exclusively determined by the interlayer coupling strength. It is worth

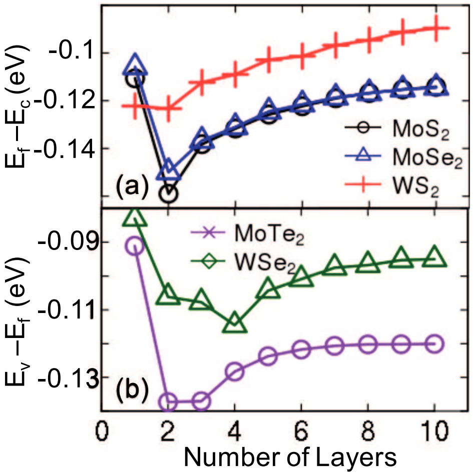

FIG. 8. Effective Fermi level $E_f - E_c$ (a) and $E_v - E_f$ (b) of n- and p-type TMD layers with varying thicknesses and for a given doping density of 1.5×10^{18} cm^{-3}, respectively.

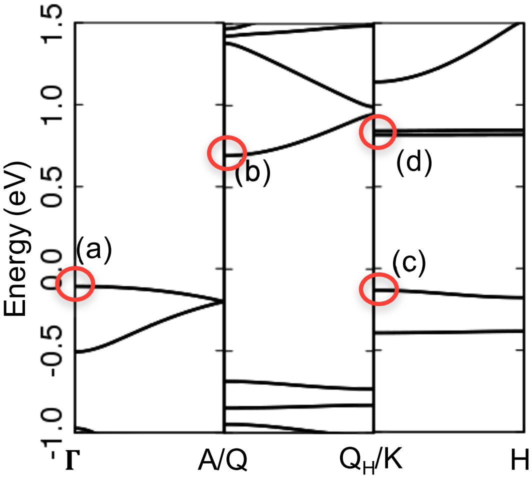

FIG. 9. $MoTe_2$ band diagram along $\vec{b_3}$ starting at the Γ, Q, and, K points defined in Fig. 4. The A, Q_H, and H points correspond to Γ, Q, and K when shifted by $\pi/c \times \vec{b_3}/|b_3|$.

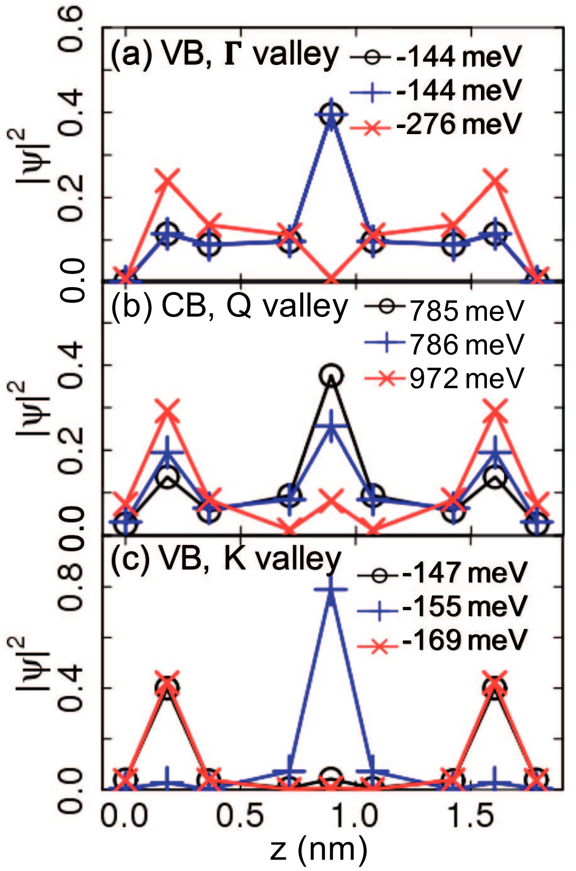

FIG. 10. Absolute squared valence band wavefunctions for the Γ valley of the valence band (a), Q valley of the conduction band (b), and K valley of the valence band (c) of a 3 layer $MoTe_2$ system corresponding to the points (a), (b), and (c) in Fig. 9, respectively. The eigenstate energy is used to label the states. Depending on the interlayer and spin orbit coupling strength, the wavefunctions are localized or delocalized. Note that the lines are meant as a guide to the eye.

emphasizing that the wave function effects discussed above are found in all considered TMD materials.

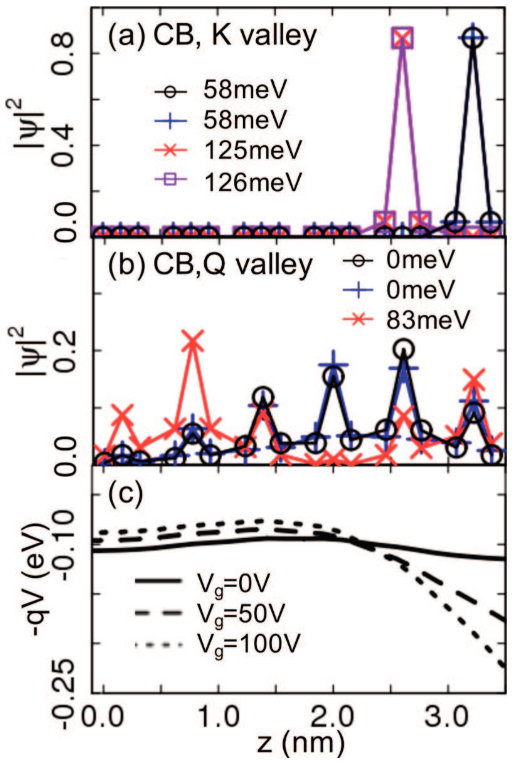

FIG. 11. Absolute squared of several conduction band wave functions at the K point (a) and at the Q point (b) for a 6-layer gated MoS_2 device depicted in Fig. 1 at a gate voltage of $V_g = 100\,V$. The MoS_2 system extends from z = 0 nm to z = 3.6 nm. The potential profiles for various gate voltages are shown in (c). The lines in (a) and (b) are meant as a guide to the eye.

E. Electric gate response

The effect of electric gates on TMD layers is exemplified with the absolute squared conduction band wave functions and the self-consistently solved electrostatic potential of a 6-layer gated MoS_2 system shown in Fig. 11. The energies of K-valley and Q-valley states get closer with the electric field: in the field free case, the bottom of K and Q valleys are separated by more than 100 meV, whereas their energy difference is about 58 meV, as seen in Fig. 11. Higher gate fields make it energetically more favorable to avoid state delocalization across the total device. This can be seen for the Q-valley states in Fig. 11(b) as their center shifts in the gate field direction. The electrostatic potential profiles for several different gate voltages are shown in Fig. 11(c). In these and all other considered cases of this work, the gate field is screened within about 1 nm penetration depth. Consequently, the thinner the TMD system is, the larger is its response to the applied gate field. This is exemplified in Fig. 12 for the effective Fermi level as a function of gate bias and layer thickness. Note that the monolayer results of this figure still assume a completely screened gate field in the vacuum, in spite of the pronounced penetration depth. Thus, the monolayer results are given for the sake of completeness only and to ease comparison with the effective Fermi levels shown in Fig. 8. For higher gate fields and TMDs thicker than the field penetration length, the gate induced shift of the effective Fermi level becomes

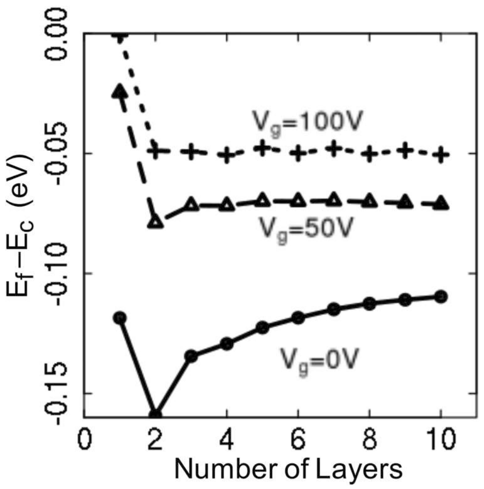

FIG. 12. Effective Fermi level of the gated MoS_2 layers shown in Fig. 1 for different thicknesses and applied gate voltages. For this comparison, a layer thickness independent doping density of $1.5 \times 10^{18}\,cm^{-3}$, is assumed.

independent of the layer thickness (see Fig. 12). Since K-valley states are localized within monolayers, they face a layer-dependent effective electric field. Accordingly, the K-valley degeneracy gets lifted by electric gates, as illustrated in Figs. 11(a) and 13. Note that the Q-valley conduction band energies and Γ valley valence band energies remain virtually unaffected by the electric gate (see Fig. 13).

F. Quantum confined Stark effect

Figure 13 also shows that the quantum confined Stark effect of the K-valley states reduces the direct band gap at the K-point. Similar effects were observed for direct band gap excitons in Refs. 23 and 61, as well as in the experiments of this work: the photoluminescence peaks of direct band gap excitons show a red-shift with increasing gate voltage (see Fig. 14). Figure 14 also shows an increase of the PL amplitude with increasing gate bias. This qualitatively agrees with the band structure results of Fig. 13: The gate field barely changes the K-valley valence band edge, but it lowers the K-valley energy of the conduction band. This results in an increase of the K-valley electron density with the gate bias, while the K-valley hole density is approximately constant. Since the photoluminescence amplitude is approximately proportional to the product of the electron and hole K-valley density (see e.g., Refs. 62 and 63), it increases with the gate bias.

It has been discussed in the literature (Refs. 21–23) whether the direct band gap excitons recombine within individual layers or across different layers [illustrated in Fig. 15(a)]. To clarify the nature of the excitons and shed more light on this question, Fig. 15(b) compares the field induced changes of the experimentally observed exciton energies with the NEMO5 results. Since the NEMO5 calculations do not include exciton binding energies, differences of K-valley conduction and valence band states of the same layer and of maximally separated layers are used to represent intralayer and interlayer excitons, respectively. For comparability of the experimental and NEMO5 results, the transition energy changes in Fig. 15(b) are shown relative to the field free case. For both the interlayer and intralayer transitions, NEMO5 predicts a finite Stark effect, but only the intralayer transition Stark effects agree qualitatively with the experimental data. Note that NEMO5 calculations of the optical

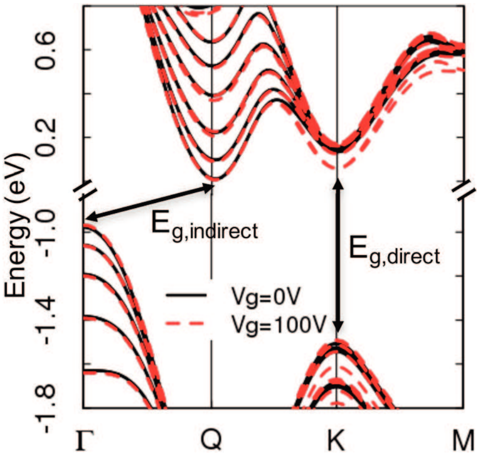

FIG. 13. Band structures of a 6-layer MoS_2 system as shown in Fig. 1 for the field free case and when a gate voltage of 100 V is applied. The gate field lifts the K valley degeneracy, while the Γ and Q valleys remain virtually unaltered. To ease the comparison, the energy offset is chosen to have the Fermi level set to 0 for both voltages.

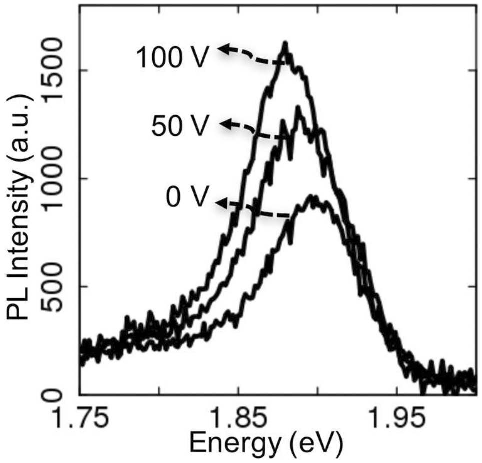

FIG. 14. Experimental photoluminescence (PL) spectra (equivalent to "peak A" in Ref. 60) of a gated 6 layer MoS_2 structure for various gate voltages. The increase of the PL amplitude with the gate voltage qualitatively agrees with the band structure changes predicted in Fig. 13 as discussed in the main text.

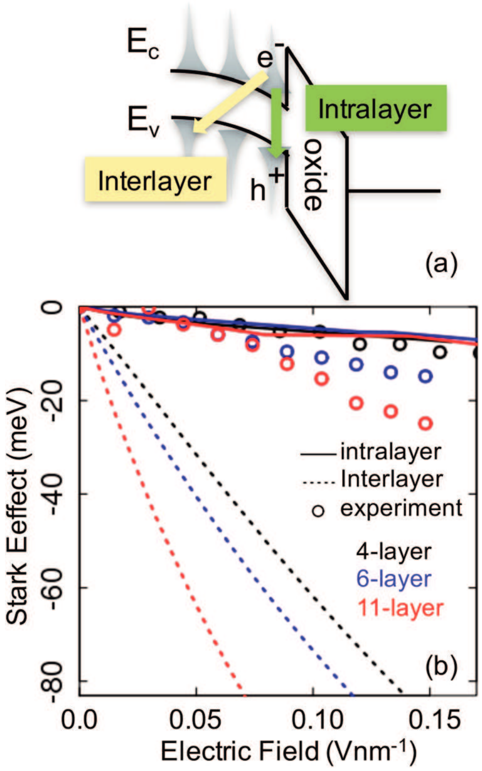

FIG. 15. (a) Schematic of the interlayer and intralayer exciton recombinations. (b) The relative change of experimentally observed direct band gap exciton energies (symbols) as a function of applied gate bias for various MoS_2 systems agrees well with the theoretically predicted energy differences of conduction and valence band K-valley states of identical layers (solid lines). In contrast, the calculated conduction and valence K-valley energy differences of maximally separated layers (dotted) significantly exceed the experimentally observed Stark effects.

matrix elements[64] (not in the figure) showed two orders of magnitude higher probability for intralayer transitions than for interlayer ones. It is also worth mentioning that our experiments did not show any Stark effect for indirect band gap excitons - in agreement with the theoretical results in Fig. 13, that show virtually gate field independent Q-valley and Γ-valley energies. In summary, these results suggest that MoS_2 excitons preferably perform intralayer transitions.

IV. CONCLUSION

Electronic wave functions and band structures in 2H-TMD structures were analyzed in the MLWF representation of the nanodevice simulation tool NEMO5. Hybridization of electronic states across multiple layers was shown to depend on the balance of spin-orbit coupling and interlayer coupling strength. This balance varies strongly with the electronic momentum. Conduction band K-valley states are found to be confined in individual monolayers. In contrast, valence band K-valley states are delocalized in equivalent layers for systems with finite spin-orbit coupling or across the total device when the spin-orbit coupling disappears. This K-state hybridization can be lifted with electric gate fields. The design range of the spin-orbit interaction, the interlayer coupling, the effective Fermi levels, and effective masses is carefully assessed. Experimental data of the quantum confined Stark effect of direct band gap, and interlayer and intralayer exciton photoluminescence were reproduced with NEMO5. Intralayer excitons were identified as the major source for photoluminescence signals—in agreement with a previous study Ref. 23.

ACKNOWLEDGMENTS

The work was supported by the NSF EFRI-1433510. We also acknowledge the Rosen Center for Advanced Computing at the Purdue University for the use of their computing resources and technical support. This research is a part of the Blue Waters sustained-petascale computing project, which is supported by the National Science Foundation (Award No. ACI 1238993) and the state of Illinois. Blue Waters is a joint effort of the University of Illinois at Urbana-Champaign and its National Center for Supercomputing Applications. This work was also a part of the Accelerating Nano-scale Transistor Innovation with NEMO5 on Blue Waters PRAC allocation support by the National Science Foundation (Award No. OCI-0832623). This work was partially supported by the National Science Foundation's MRSEC program (DMR-1121262) and made use of its Shared Facilities at the Materials Research Center of the Northwestern University. This work made use of the EPIC facility of the Northwestern University's NU*ANCE* Center and the NUFAB facility, which have received support from the Soft and Hybrid Nanotechnology Experimental (SHyNE) Resource (NSF ECCS-1542205), the MRSEC program (NSF DMR-1121262) at the Materials Research Center, the International Institute for Nanotechnology (IIN), the Keck Foundation, and the State of Illinois. N.P.S. acknowledges support as an Alfred P. Sloan Research Fellow. J.M. acknowledges support from the NSERC.

[1] K. S. Novoselov, D. Jiang, F. Schedin, T. J. Booth, V. V. Khotkevich, S. V. Morozov, and A. K. Geim, "Two-dimensional atomic crystals," Proc. Natl. Acad. Sci. U.S.A. **102**, 10451 (2005).

[2] B. Radisavljevic, A. Radenovic, J. Brivio, V. Giacometti, A. Kis, B. Radisavljevic, A. Radenovic, J. Brivio, V. Giacometti, and A. Kis, "Single-layer MoS_2 transistors," Nat. Nanotechnol. **6**, 147 (2011).

[3] W. S. Yun, S. Han, S. C. Hong, I. G. Kim, and J. Lee, "Thickness and strain effects on electronic structures of transition metal dichalcogenides: 2H-MX_2 semiconductors (M = Mo, W; X = S, Se, Te)," Phys. Rev. B **85**, 1 (2012).

[4] C. Zhu, D. Du, and Y. Lin, "Graphene-like 2D nanomaterial-based biointerfaces for biosensing applications," Biosens. Bioelectron. **89**, 43 (2017).

[5] D. Jariwala, V. K. Sangwan, L. J. Lauhon, T. J. Marks, and M. C. Hersam, "Emerging device applications for semiconducting two-dimensional transition metal dichalcogenides," ACS Nano **8**, 1102 (2014).

[6] K. Kalantar-zadeh and J. Z. Ou, "Biosensors based on two-dimensional MoS_2," ACS Sens. **1**, 5 (2016).

[7] M. R. Esmaeili-Rad and S. Salahuddin, "High performance molybdenum disulfide amorphous silicon heterojunction photodetector," Sci. Rep. **3**, 2345 (2013).

[8] J. S. Ross, P. Klement, A. M. Jones, N. J. Ghimire, J. Yan, M. G. T. Taniguchi, K. Watanabe, K. Kitamura, W. Yao, D. H. Cobden, and X. Xu, "Electrically tunable excitonic light-emitting diodes based on monolayer WSe_2 p-n junctions," Nat. Nanotechnol. **9**, 268 (2014).

[9] M. S. Choi, D. Qu, D. Lee, X. Liu, K. Watanabe, T. Taniguchi, and W. J. Yoo, "Lateral MoS_2 p-n junction formed by chemical doping for use in high-performance optoelectronics," ACS Nano **8**, 9332 (2014).

[10] F. Withers, O. Del Pozo-Zamudio, A. Mishchenko, A. P. Rooney, A. Gholinia, K. Watanabe, T. Taniguchi, S. J. Haigh, A. K. Geim, A. I. Tartakovskii, and K. S. Novoselov, "Light-emitting diodes by band-structure engineering in van der Waals heterostructures," Nat. Mater. **14**, 301 (2015).

[11] S. Bertolazzi, D. Krasnozhon, and A. Kis, "Nonvolatile memory cells based on MoS_2/graphene heterostructures," ACS Nano **7**, 3246 (2013).

[12] V. K. Sangwan, D. Jariwala, I. S. Kim, K.-S. Chen, T. J. Marks, L. J. Lauhon, and M. C. Hersam, "Gate-tunable memristive phenomena mediated by grain boundaries in single-layer MoS_2," Nat. Nanotechnol. **10**, 403 (2015).

[13] Z. Q. Zheng, T. M. Zhang, J. D. Yao, Y. Zhang, J. R. Xu, and G. W. Yang, "Flexible, transparent and ultra-broadband photodetector based on large-area WSe_2 film for wearable devices," Nanotechnology **27**, 11 (2016).

[14] J. Y. Oh, J. H. Lee, S. W. Han, S. S. Chae, E. J. Bae, Y. H. Kang, W. J. Choi, S. Y. Cho, J.-O. Lee, H. K. Baik, and T. I. Lee, "Chemically exfoliated transition metal dichalcogenide nanosheet-based wearable thermoelectric generators," Energy Environ. Sci. **9**, 1696 (2016).

[15] F. Bonaccorso, A. Lombardo, T. Hasan, Z. Sun, L. Colombo, and A. C. Ferrari, "Production, processing and placement of graphene and two dimensional crystals," Mater. Today **15**, 564 (2012).

[16] L. Britnell, R. M. Ribeiro, A. Eckmann, R. Jalil, B. D. Belle, A. Mishchenko, Y.-J. Kim, R. V. Gorbachev, T. Georgiou, S. V. Morozov, A. N. Grigorenko, A. K. Geim, C. Casiraghi, A. H. C. Neto, and K. S. Novoselov, "Strong light-matter interactions in heterostructures of atomically thin films," Science **340**, 1311 (2013).

[17] A. K. Geim and I. V. Grigorieva, "Van der Waals heterostructures," Nature **499**, 419 (2014).

[18] S. L. Howell, D. Jariwala, C. C. Wu, K. S. Chen, V. K. Sangwan, J. Kang, T. J. Marks, M. C. Hersam, and L. J. Lauhon, "Investigation of band-offsets at monolayer-multilayer MoS_2 junctions by scanning photocurrent microscopy," Nano Lett. **15**, 2278 (2015).

[19] F. W. Chen, H. Ilatikhameneh, T. A. Ameen, G. Klimeck, and R. Rahman, "Thickness engineered tunnel field-effect transistors based on phosphorene," IEEE Electron Device Lett. **38**, 130 (2017).

[20] X. Zhu, N. R. Monahan, Z. Gong, H. Zhu, K. W. Williams, and C. A. Nelson, "Charge transfer excitons at van der Waals interfaces," J. Am. Chem. Soc. **137**, 8313 (2015).

[21] H. Chen, X. Wen, J. Zhang, T. Wu, Y. Gong, X. Zhang, J. Yuan, C. Yi, J. Lou, P. M. Ajayan, W. Zhuang, G. Zhang, and J. Zheng, "Ultrafast formation of interlayer hot excitons in atomically thin MoS_2/WS_2 heterostructures," Nat. Commun. **7**, 12512 (2016).

[22] T. Chu, H. Ilatikhameneh, G. Klimeck, R. Rahman, and Z. Chen, "Electrically tunable bandgaps in bilayer MoS_2," Nano Lett. **15**, 8000 (2015).

[23] J. Klein, J. Wierzbowski, A. Regler, J. Becker, F. Heimbach, K. Müller, M. Kaniber, and J. J. Finley, "Stark effect spectroscopy of mono- and few-layer MoS_2," Nano Lett. **16**, 1554 (2016).

[24] N. Marzari, A. A. Mostofi, J. R. Yates, I. Souza, and D. Vanderbilt, "Maximally localized Wannier functions: Theory and applications," Rev. Mod. Phys. **84**, 1419 (2012).

[25] Á. Szabó, R. Rhyner, and M. Luisier, "Ab initio simulation of single- and few-layer MoS_2 transistors: Effect of electron-phonon scattering," Phys. Rev. B - Condens. Matter Mater. Phys. **92**, 035435 (2015).

[26] H. Ilatikhameneh, Y. Tan, B. Novakovic, G. Klimeck, R. Rahman, and J. Appenzeller, "Tunnel field-effect transistors in 2-D transition metal dichalcogenide materials," IEEE J. Explor. Solid-State Comput. Devices Circuits **1**, 12 (2015).

[27] S. Fang, R. Kuate Defo, S. N. Shirodkar, S. Lieu, G. A. Tritsaris, and E. Kaxiras, "*Ab initio* tight-binding Hamiltonian for transition metal dichalcogenides," Phys. Rev. B - Condens. Matter Mater. Phys. **92**, 205108 (2015).

[28] J. Maassen, M. Harb, V. Michaud-Rioux, Y. Zhu, and H. Guo, "Quantum transport modeling from first principles," Proc. IEEE **101**, 518 (2013).

[29] See http://cms.mpi.univie.ac.at/vasp/vasp.pdf for 6.67.3 Finite electric fields applications (2015).

[30] See http://www.arscryo.com/CS204_F-DMX-20-OM.html for equipment details (2016).

[31] See http://www.andor.com/spectrograph/shamrock-spectrograph-series/shamrock-303i for equipment details (2016).

[32] S. Steiger, M. Povolotskyi, H. H. Park, T. Kubis, and G. Klimeck, "NEMO5: A parallel multiscale nanoelectronics modeling tool," IEEE Trans. Nanotechnol. **10**, 1464 (2011).

[33] G. Kresse and J. Furthmüller, "Efficient iterative schemes for ab initio total-energy calculations using a plane-wave basis set," Phys. Rev. B **54**, 11169 (1996).

[34] T. Bučko, J. Hafner, S. Lebègue, and J. G. Ángyán, "Improved description of the structure of molecular and layered crystals: Ab initio DFT calculations with van der Waals corrections," J. Phys. Chem. A **114**, 11814 (2010).

[35] F. Jellinek, G. Brauer, and H. Müller, "Molybdenum and niobium sulphides," Nature **185**, 376 (1960).

[36] W. Wei, Y. Dai, C. Niu, and B. Huang, "Controlling the electronic structures and properties of in-plane transition-metal dichalcogenides quantum wells," Sci. Rep. **5**, 17578 (2015).

[37] J. P. Perdew, K. Burke, and Y. Wang, "Generalized gradient approximation for the exchange-correlation hole of a many-electron system," Phys. Rev. B **54**, 16533 (1996).

[38] N. Marzari and D. Vanderbilt, "Maximally-localized generalized Wannier functions for composite energy bands," Phys. Rev. B **56**, 12847 (1997).

[39] K. S. Thygesen, L. B. Hansen, and K. W. Jacobsen, "Partly occupied Wannier functions: Construction and applications," Phys. Rev. B **72**, 125119 (2005).

[40] R. Das, S. K. Pandey, and P. Mahadevan, "Layer dependent electronic structure changes in transition metal dichalcogenides-The role of geometric confinement," e-print arXiv.org/abs/1702.04535 (2017).

[41] D. Jariwala, V. K. Sangwan, D. J. Late, J. E. Johns, V. P. Dravid, T. J. Marks, L. J. Lauhon, and M. C. Hersam, "Band-like transport in high mobility unencapsulated single-layer MoS_2 transistors," Appl. Phys. Lett. **102**, 173107 (2013).

[42] S. Saito, K. Torii, M. Hiratani, and T. Onai, "Analytical quantum mechanical model for accumulation capacitance of MOS structures," IEEE Electron Device Lett. **23**, 348 (2002).

[43] A. Novikov, "Experimental measurement of work function in doped silicon surfaces," Solid State Electron. **54**, 8 (2010).

[44] X. Chen, Z. Wu, S. Xu, L. Wang, R. Huang, Y. Han, W. Ye, W. Xiong, T. Han, G. Long, Y. Wang, Y. He, Y. Cai, P. Sheng, and N. Wang, "Probing the electron states and metal-insulator transition mechanisms in molybdenum disulphide vertical heterostructures," Nat. Commun. **6**, 6088 (2015).

[45] P. Sarangapani, D. Mejia, J. Charles, W. Gilbertson, H. Ilatikhameneh, T. Ameen, A. Roche, J. Fonseca, and G. Klimeck, in *2015 International Workshop on Computational Electronics* (2015), pp. 1–3.

[46] K. Liu, L. Zhang, T. Cao, C. Jin, D. Qiu, Q. Zhou, A. Zettl, P. Yang, S. G. Louie, and F. Wang, "Evolution of interlayer coupling in twisted molybdenum disulfide bilayers," Nat. Commun. **5**, 4966 (2014).

[47] L. Zhang and A. Zunger, "Evolution of electronic structure as a function of layer thickness in group-VIB transition metal dichalcogenides: Emergence of localization prototypes," Nano Lett. **15**, 949 (2015).

[48] J. Kang, L. Zhang, and S. H. Wei, "A unified understanding of the thickness-dependent bandgap transition in hexagonal two-dimensional semiconductors," J. Phys. Chem. Lett. **7**, 597 (2016).

[49] H.-M. Li, D. Lee, D. Qu, X. Liu, J. Ryu, A. Seabaugh, and W. J. Yoo, "Ultimate thin vertical p-n junction composed of two-dimensional layered molybdenum disulfide," Nat. Commun. **6**, 6564 (2015).

[50] Y. Jin, D. H. Keum, S. J. An, J. Kim, H. S. Lee, and Y. H. Lee, "A Van der Waals homojunction: Ideal p-n diode behavior in $MoSe_2$," Adv. Mater. **27**, 5534 (2015).

[51] D. Ovchinnikov, A. Allain, Y. S. Huang, D. Dumcenco, and A. Kis, "Electrical transport properties of single-layer WS_2," ACS Nano **8**, 8174 (2014).

[52] J. Wilson and A. Yoffe, "The transition metal dichalcogenides discussion and interpretation of the observed optical, electrical and structural properties," Adv. Phys. **18**, 193 (1969).

[53] R. Akashi, M. Ochi, S. Bordács, R. Suzuki, Y. Tokura, Y. Iwasa, and R. Arita, "Two-dimensional valley electrons and excitons in noncentrosymmetric 3R-MoS_2," Phys. Rev. Appl. **4**, 014002 (2015).

[54] Y. Li, Y. Rao, K. F. Mak, Y. You, S. Wang, C. R. Dean, and T. F. Heinz, "Probing symmetry properties of few-layer MoS_2 and h-BN by optical second-harmonic generation," Nano Lett. **13**, 3329 (2013).

[55] K. Kośmider, J. W. González, and J. Fernández-Rossier, "Large spin splitting in the conduction band of transition metal dichalcogenide monolayers," Phys. Rev. B - Condens. Matter Mater. Phys. **88**, 1 (2013).

[56] J. R. Schaibley, H. Yu, G. Clark, P. Rivera, J. S. Ross, K. L. Seyler, W. Yao, and X. Xu, "Valleytronics in 2D materials," Nat. Rev. Mater. **1**, 16055 (2016).

[57] A. M. Jones, H. Yu, J. S. Ross, P. Klement, N. J. Ghimire, J. Yan, D. G. Mandrus, W. Yao, and X. Xu, "Spin-layer locking effects in optical orientation of exciton spin in bilayer WSe_2," Nat. Phys. **10**, 130 (2014).

[58] Z. Gong, G.-B. Liu, H. Yu, D. Xiao, X. Cui, X. Xu, and W. Yao, "Magnetoelectric effects and valley-controlled spin quantum gates in transition metal dichalcogenide bilayers," Nat. Commun. **4**, 2053 (2013).

[59] X. Xu, W. Yao, D. Xiao, and T. F. Heinz, "Spin and pseudospins in layered transition metal dichalcogenides," Nat. Phys. **10**, 343 (2014).

[60] K. F. Mak, C. Lee, J. Hone, J. Shan, and T. F. Heinz, "Atomically thin MoS_2: A new direct-gap semiconductor," Phys. Rev. Lett. **105**, 136805 (2010).

[61] J. G. Kim, W. S. Yun, S. Jo, J. Lee, and C.-H. Cho, "Effect of interlayer interactions on exciton luminescence in atomic-layered MoS_2 crystals," Sci. Rep. **6**, 29813 (2016).

[62] J. Piprek, "Efficiency droop in nitride-based light-emitting diodes," Phys. Status Solidi A **207**, 2217 (2010).

[63] R. N. Hall, "Electron-hole recombination in germanium," Phys. Rev. **87**, 387 (1952).

[64] S. L. Chuang, *Physics of Optoelectronic Devices, Wiley Series in Pure and Applied Optics* (Wiley, 1995).